APPLIED PHYSICS

# Cavity magnomechanics

Xufeng Zhang,[1] Chang-Ling Zou,[1,2] Liang Jiang,[2] Hong X. Tang[1,2]*


10.1126/sciadv.1501286

**A dielectric body couples with electromagnetic fields through radiation pressure and electrostrictive forces, which mediate phonon-photon coupling in cavity optomechanics. In a magnetic medium, according to the Korteweg-Helmholtz formula, which describes the electromagnetic force density acting on a medium, magneostrictive forces should arise and lead to phonon-magnon interaction. We report such a coupled phonon-magnon system based on ferrimagnetic spheres, which we term as cavity magnomechanics, by analogy to cavity optomechanics. Coherent phonon-magnon interactions, including electromagnetically induced transparency and absorption, are demonstrated. Because of the strong hybridization of magnon and microwave photon modes and their high tunability, our platform exhibits new features including parametric amplification of magnons and phonons, triple-resonant photon-magnon-phonon coupling, and phonon lasing. Our work demonstrates the fundamental principle of cavity magnomechanics and its application as a new information transduction platform based on coherent coupling between photons, phonons, and magnons.**

## INTRODUCTION

Mechanical oscillators have been recently widely studied as a transducer mediating the coherent signal conversion between different systems (*1*). Particularly, radiation force (*2*–*13*), electrostatic force (*14*–*16*), and piezoelectric force (*17*, *18*) have been used for coupling phonon with optical or microwave photons. Such interaction mechanisms lead to the fast development of a variety of cavity electro- and optomechanical systems (*1*), but they all intrinsically lack good tunability. The magnetostrictive force (*19*) provides an alternative mechanism to allow a different information carrier—magnon—to couple with phonon. Magnon is a collective excitation of magnetization, whose frequency can be tuned at will by adjusting the bias magnetic field (*20*–*22*). The magnetostrictive interaction has long been overlooked for information processing because it is negligibly weak in commonly used dielectric or metallic materials. However, in magnetic materials, the magnetostrictive force becomes dominant, which provides a great opportunity to establish a highly tunable hybrid system for coherent information processing (*23*, *24*). Recent advances in ultrafast optics can even allow the study and application of such systems in the picosecond time scale (*25*–*29*). Among all the magnetic materials, the magnetic insulator yttrium iron garnet (YIG, $Y_3Fe_5O_{12}$) has excellent material properties. For instance, YIG is well known for its rich magnonic nonlinearities. Besides, YIG has very low loss for various different information carriers, including magnon, acoustic phonon, and microwave photon. Moreover, as a dielectric, YIG is transparent for infrared light. All these properties would enable further integration of the magnonic systems with opto- or electromechanical elements, providing an excellent platform for quantum state transfer among different physical systems.

Here, we demonstrate an intriguing cavity magnomechanical system in which magnon couples with phonon through magnetostrictive interaction, resulting in magnomechanically induced transparency/absorption (MMIT/MMIA) and magnomechanical parametric amplication (MMPA). MMIT/MMIA are hallmark coherent phenomena in analogy to the recent optomechanical observations (*2*, *5*, *6*, *30*), which have not been observed in previous studies of parametric magnetoelastic systems (*23*, *24*). During such processes, uniform magnon modes (the ferromagnetic resonance precession) are in the hybridized state with cavity microwave photons because they are strongly coupled to each other (*31*–*35*). Therefore, coherent signal conversions among these three different information carriers are realized in a single device. The magnetic field dependence of magnon provides our system with unprecedented tunability compared with opto- or electromechanical systems. Moreover, the great flexibility of this system allows us to achieve triple resonance among magnon, phonon, and photon, which drastically enhances the magnomechanical interaction. The principles demonstrated in our room temperature experiments can be readily applied to the quantum regime at millikelvin temperature, opening up great opportunities in various applications such as tunable microwave filter and amplifier (*36*), long-lifetime quantum memories (*37*), and microwave-to-optics conversion (*15*).

## RESULTS

The device used in our experiments is schematically shown in Fig. 1A. The key component is a highly polished single-crystal YIG sphere glued to the end of a silica fiber for supporting purpose (Fig. 1B). With an external magnetic field $H$ biased along the $z$ direction, a uniform magnon mode resonates in the YIG sphere at frequency $\omega_m = \gamma H$, where $\gamma$ is the gyromagnetic ratio. The YIG sphere is also an excellent mechanical resonator (Fig. 1C), owing to its superior material and geometrical properties. The varying magnetization induced by the magnon excitation inside the YIG sphere causes deformation of its spherical geometry (and vice versa), introducing the coupling between magnon and phonon modes (Fig. 1D). Considering the large frequency mismatch between the magnon and the phonon modes (gigahertz versus megahertz) with our experiment parameters, a strong parametric drive is used to compensate for their frequency difference. In this case, the system is described by a radiation pressure–like, dispersive interaction Hamiltonian (see the Supplementary Materials) $\mathcal{H} = \hbar g_{mb} \hat{m}^\dagger \hat{m} (\hat{b} + \hat{b}^\dagger)$, where $\hbar$ is the reduced Planck's constant, $\hat{b}$ ($\hat{m}$) is the boson operator of the phonon (magnon) mode, and $g_{mb}$ is the single magnon-phonon coupling strength.

The magnetostrictive coupling strength is determined by the mode overlap between the uniform magnon mode and the phonon modes. In a YIG sphere, there exist various phonon modes, each with a different displacement profile and, consequently, a different coupling strength with the magnon mode. Figure 2A plots the typical profiles of the lowest order spheroidal phonon modes $S_{1,l,m_a}$ ($l$ and $m_a$ are the angular and azimuthal mode numbers, respectively), among which the $S_{1,2,2}$ mode

[1]Department of Electrical Engineering, Yale University, New Haven, CT 06511, USA.
[2]Department of Applied Physics, Yale University, New Haven, CT 06511, USA.
*Corresponding author. E-mail: hong.tang@yale.edu

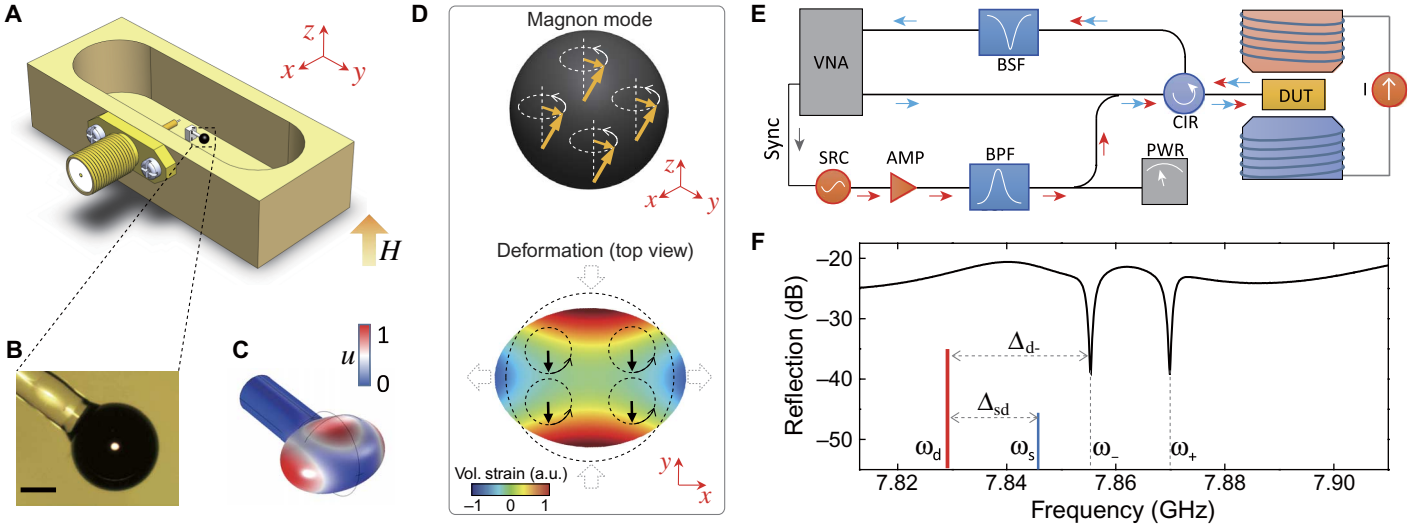


**Fig. 1. Device schematic and measurement setup.** (**A**) Schematic of the device that consists of a three-dimensional copper cavity (only bottom half is shown) and a YIG sphere. The YIG sphere is placed near the maximum microwave magnetic field (along the *y* direction) of the cavity $TE_{011}$ mode. A uniform external magnetic field (*H*) is applied along the *z* direction to bias the YIG sphere for magnon-photon coupling. (**B**) Optical image of the highly polished 250-μm-diameter YIG sphere that is glued to a 125-μm-diameter supporting silica fiber. The gluing area is minimized to reduce the contact damping to the phonon mode. Scale bar, 100 μm. (**C**) Simulated mechanical displacement (*u*) of the $S_{1,2,2}$ phonon mode in the YIG sphere that has the strongest magnomechanical interaction with the uniform magnon mode. (**D**) An intuitive illustration of the magnomechanical coupling. Top panel shows the uniform magnon excitation in the YIG sphere. Bottom panel illustrates how the dynamic magnetization of magnon (vertical black arrows) causes the deformation (compression along the *y* direction) of the YIG sphere (and vice versa), which rotates at the magnon frequency. The color scale represents the corresponding volumetric strain fields induced by the dynamic magnetization of magnon. In our experiments, we excite the magnon at gigahertz frequencies and the phonon mode is actuated parametrically, that is, at the beating frequencies (megahertz) of two magnon modes. (**E**) Schematic illustration of the measurement setup. VNA, vector network analyzer; SRC, microwave source for driving; AMP, microwave amplifier; BPF, bandpass filter; PWR, microwave power meter; CIR, circulator; BSF, bandstop filter; DUT, device under test. (**F**) Black curve: Cavity reflection spectrum when magnon is on-resonance with the cavity photon mode. The two dips represent the maximum hybridized modes $\hat{A}_{\pm} = \frac{1}{\sqrt{2}}(\hat{a} \pm \hat{m})$. Red and blue vertical lines indicate the applied drive and probe, respectively. The probe is swept across the hybrid mode resonance. $\Delta_{sd}$, two-photon (probe-drive) detuning; $\Delta_{d-}$, drive-resonance detuning.

shows the highest coupling strength when the bias field is along the direction of maximum displacement (Fig. 2B). Therefore, in our experiments, we focus only on the $S_{1,2,2}$ mode. Although a YIG sphere with a smaller diameter is favorable for achieving larger coupling strengths (Fig. 2B), it also results in a higher frequency for the phonon mode (Fig. 2C), which in turn leads to lower responsivity to the parametric drive, so a trade-off has to be made when choosing the sphere size. In our experiments, a 250-μm-diameter YIG sphere is used, corresponding to a phonon frequency $\omega_b/2\pi$ = 11.42 MHz and a coupling strength $g_{mb}/2\pi \leq 9.9$ mHz. With an external drive of 0 dBm, the linear magnon-phonon coupling can be enhanced to around 30 kHz, which is two orders of magnitude larger than the phonon dissipation rate, $\kappa_b$.

Magnetostriction mediates the coupling between magnons and photons. However, to achieve coherent magnon-phonon coupling, it is further required that the phonon mode should have a relatively long lifetime. Single-crystal YIG has a garnet structure that is known to exhibit very low mechanical damping and therefore supports a material-limited phonon lifetime over a millisecond (*38*). The supporting fiber that is glued to the YIG sphere reduces the phonon lifetime (Fig. 2D). In our experiments, the measured linewidth of $S_{1,2,2}$ phonon mode with a 125-μm-diameter supporting fiber is $2\kappa_b/2\pi$ = 300 Hz, which is sufficiently small for observing coherent magnon-phonon coupling phenomena.

Figure 1E plots the schematics of our measurement setup at room temperature ambient condition. The YIG sphere is placed inside a three-dimensional microwave cavity (Fig. 1A). A weak probe signal is sent into the cavity through a coaxial probe, and by sweeping its frequency $\omega_s$ and measuring the reflection, we can infer the interaction among photon, magnon, and phonon inside the cavity. The YIG sphere is positioned at the maximum microwave magnetic field of the cavity $TE_{011}$ mode, which resonates at $\omega_a/2\pi$ = 7.86 GHz. By controlling the bias magnetic field, we tune the magnon close to the resonance with the cavity photon mode. This leads to the hybridization between magnon and photon (*31*–*34*), which shows up in the reflection spectrum as a pair of split normal modes (Fig. 1F). Because each of the two hybrid modes contains magnon components, it coherently couples with the phonon modes when the cavity is parametrically driven by a strong microwave signal at $\omega_d$.

We first study each individual hybrid mode for its coherent magnomechanical coupling by applying an off-resonance microwave drive and ignoring processes that simultaneously involve both hybrid modes. In this case, the cavity magnomechanical system can be described by

$$\mathcal{H}_{mb,1} = \hbar g_{mb}(\hat{b} + \hat{b}^{\dagger})(\sin^2\theta \hat{A}_+^{\dagger}\hat{A}_+ + \cos^2\theta \hat{A}_-^{\dagger}\hat{A}_-) \qquad (1)$$

where the two hybrid modes interact with the phonon mode independently. Here, $\hat{A}_+ = \cos\theta\hat{a} + \sin\theta\hat{m}$ and $\hat{A}_- = -\sin\theta\hat{a} + \cos\theta\hat{m}$ are quantized boson operators for hybridized excitations constituted by the magnon and microwave photon ($\hat{a}$), where $\theta = \frac{1}{2}\arctan\frac{2g_{ma}}{\Delta_{ma}}$ varies

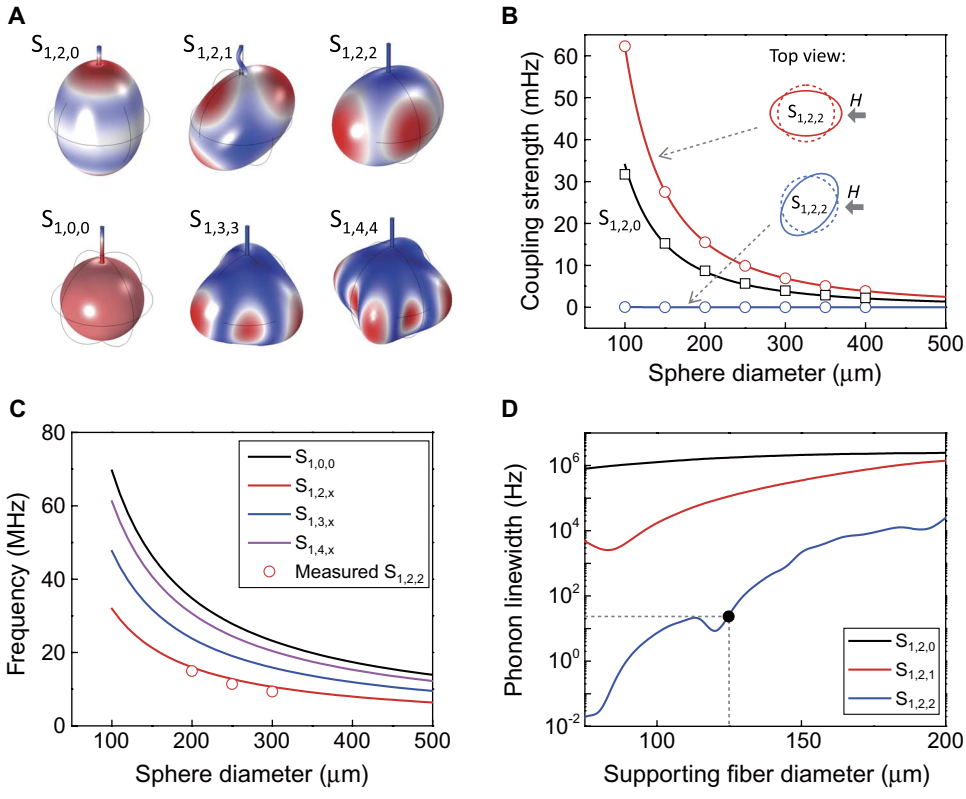


**Fig. 2. Analysis of the phonon modes and magnetostrictive coupling strengths.** (**A**) Simulated displacement profiles of the low-order phonon modes in the YIG sphere (with a small supporting fiber). $S_{1,l,m_a}$ represents the spheroidal mode with a radial mode number of 1, an angular mode number of *l*, and an azimuthal mode number of $m_a$. (**B**) Theoretical prediction of the magnomechanical coupling strength as a function of YIG sphere diameter for the $S_{1,2,0}$ (black) and $S_{1,2,2}$ modes (red and blue, corresponding to different bias field directions). Solid lines are numerical calculations, whereas symbols are analytical fittings. (**C**) Phonon mode frequency as a function of the YIG sphere diameter. Solid lines are the theoretical calculations, showing an inverse proportional dependence, whereas red circles are the measurement results. (**D**) Simulated phonon linewidth due to clamping loss as a function of the supporting fiber diameter for the $S_{1,2,m_a}$ modes. Black dot indicates the experiment parameter, showing an anchor loss–limited linewidth of 20 Hz.

with photon-magnon coupling strength $g_{ma}$ and photon-magnon detuning $\Delta_{ma} = \omega_m - \omega_a$. In our system, both the magnon and the cavity photon modes have a relatively narrow linewidth ($2\kappa_m/2\pi$ = 1.12 MHz and $2\kappa_a/2\pi$ = 3.35 MHz). As a result, the hybrid mode linewidth is well below the phonon frequency, leading our system deep inside the resolved sideband regime, by analogy with optomechanical systems (*1*). In this case, the nonlinear interaction can be converted either into the linear beam splitter model $\hbar(G_\pm \hat{A}_\pm^\dagger \hat{b} + G_\pm^* \hat{A}_\pm \hat{b}^\dagger)$ or the parametric oscillator model $\hbar(G_\pm \hat{A}_\pm^\dagger \hat{b}^\dagger + G_\pm^* \hat{A}_\pm \hat{b})$ with the presence of an external drive, where $G_\pm = A_{\pm,ss} g_{mb}(1 \mp \cos 2\theta)/2$ is the enhanced coupling strength and $A_{\pm,ss}$ is the steady state amplitude of the hybrid mode, corresponding to the effective pumping of the microwave drive on magnon due to the magnon-photon hybridization (see the Supplementary Materials). Note that $\hat{A}_\pm$ are the shifted operators, and we use the same symbols as the unshifted situations for clarity and simplicity.

Figure 3, A and B, plots the measured reflection spectra for a series of bias magnetic fields with a microwave drive at a fixed frequency, $\omega_d$. To avoid the influence of the other hybrid mode, the driving signal is red (blue)–detuned for the lower (upper) hybrid mode, as illustrated in the top insets. For the red-detuned drive, the power is held constant at 26 dBm. In the spectra, the broad Lorentzian-shaped resonance dip corresponds to the hybrid mode $\hat{A}_-$, whereas the very sharp modification of the spectra at the two-photon detuning $\Delta_{sd} = \omega_b$ is evidence of coherent magnomechanical interaction. The zoomed-in spectra in Fig. 3A show that these phonon-induced resonances have a Fano-like shape that varies with the bias magnetic field. When the drive-resonance detuning $\Delta_{d-} = \omega_d - \omega_- = -\omega_b$, the Fano-like resonance changes into a symmetric Lorentzian-shaped transparency peak (MMIT). In contrast, the Fano-like resonances in the spectra for the blue-detuned drive (with a constant power of 22 dBm) show an opposite symmetry (Fig. 3B). When the drive is blue-detuned to $\Delta_{d+} = \omega_d - \omega_+ = \omega_b$, such a resonance becomes a Lorentzian-shaped absorption dip (MMIA).

One distinct advantage of magnon is that its frequency is determined by the external bias magnetic field and therefore can be conveniently tuned in a broad range. By varying $\Delta_{ma}$, the percentage of magnon component in the hybrid mode changes. Therefore, the hybrid mode experiences different effective dissipation rate, external coupling rate, and effective coupling strength with the phonon mode. As a result, the coherent magnomechanical interaction is magnetically controllable, which can be quantified by the dependence of the cooperativity $C = G_\pm^2/\kappa_\pm\kappa_b$ on the bias magnetic field. The measured *C*-*H* relation is plotted in Fig. 3D. For each measurement under a specific bias condition, the drive frequency is detuned from the hybrid mode

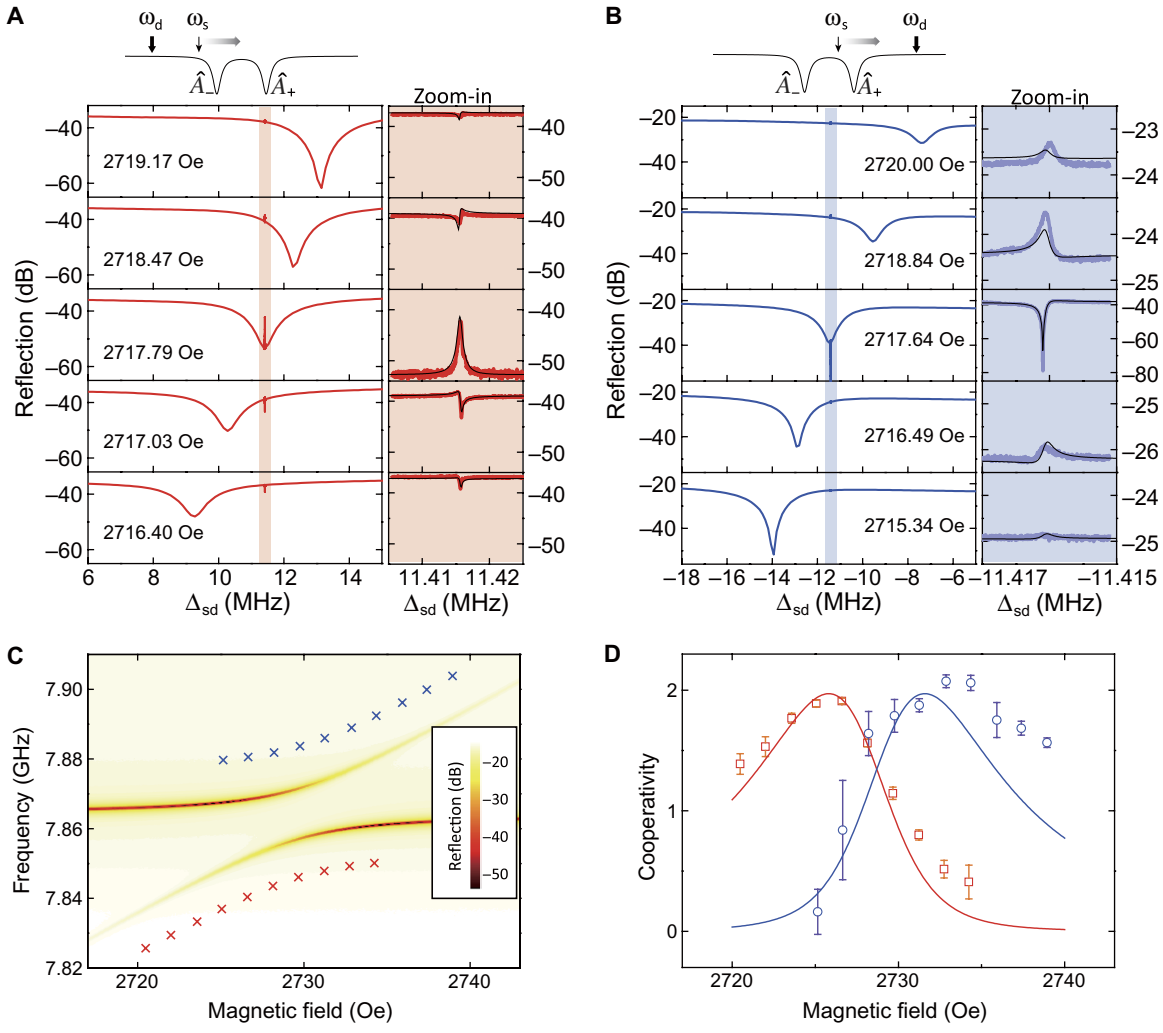


**Fig. 3. Tunable MMIT/MMIA.** (**A**) Measured reflection spectra near the lower hybrid mode $\hat{A}_-$ as a function of the two-photon detuning $\Delta_{sd}$ for a series of different bias magnetic fields. The broad dip corresponds to the lower hybrid mode resonance, whose line shape changes with bias magnetic field because of the change in the ratio between magnon and photon components. A strong (26 dBm) microwave drive is red-detuned with a fixed driving frequency $\omega_d$. A Fano-like narrow resonance line shows up inside the hybrid mode, which turns into a Lorentzian transparency peak when $\Delta_{d-} = -\omega_b$. Zoom-in shows detailed spectra of the magnomechanically induced resonances [shaded area in (A)]. (**B**) Measured reflection spectra near the upper hybrid mode $\hat{A}_+$ with a blue-detuned strong drive (22 dBm) for various bias magnetic fields. When $\Delta_{d+} = \omega_b$, the magnomechanically induced narrow resonance shows up as a Lorentzian absorption dip. Zoom-in shows detailed spectra of the shaded area in (B). (**C**) Reflection spectra of the hybrid magnon-photon modes at various bias magnetic fields. The crosses indicate the drive frequency and bias magnetic field used for each data point in (D). (**D**) The magnomechanical cooperativity as a function of bias magnetic field. For each measurement, the microwave drive is detuned from the hybrid mode by $\Delta_{d\pm} = \pm\omega_b$, while the probe is swept across the hybrid mode resonance. Red squares (blue circles) are for the red (blue) detuning situation. Solid lines in (D) and in the zoom-in of (A) and (B) are theoretical calculations using only a single-fitting parameter $g_{mb}$.

by $\Delta_{d\pm} = \pm\omega_b$, as indicated by the crosses in Fig. 3C, while the driving power is fixed constant at 30 dBm. We observed that there exists an optimal condition for a maximum $C$, as a result of the competition between the magnon and photon components in the hybrid mode: more magnon component yields stronger magnetostrictive coupling, whereas more photon component leads to a higher driving efficiency. From these measurement results, we can extract the magnon-phonon coupling strength $g_{mb}/2\pi = 4.1$ mHz, in accordance with our theoretical prediction (Fig. 2B).

The great flexibility of our system leads to tremendous advantages. For instance, it allows us to work under the interesting triple-resonance condition, where both maximum hybridized modes simultaneously couple with the phonon mode, as described by

$$\mathcal{H}_{mb,2} = \frac{1}{2}\hbar g_{mb}\left(\hat{b} + \hat{b}^\dagger\right)\left(\hat{A}_+^\dagger\hat{A}_- + \hat{A}_-^\dagger\hat{A}_+\right) \quad (2)$$

Here, we tune the magnon mode to be on resonance with the microwave cavity mode, and therefore, the two hybrid modes contain equal amounts of magnon and photon and have equal dissipation rates ($\kappa = \kappa_+ = \kappa_-$). By adjusting the direction of bias field or the position of the

YIG sphere inside the cavity, we can tune the hybrid mode splitting to match the phonon frequency $\omega_b$. In this case, both the drive and probe photons can be applied on-resonance with the hybrid modes (top inset of Fig. 4, A and B), resulting in a drastically enhanced magnomechanical coupling. For the red-detuned drive, the transparency windows at various driving powers are plotted in Fig. 4A. In addition to the red shift of the center frequency, the linewidth of the transparency windows exhibits a clear linear dependence on the driving power (Fig. 4C, red squares). With a driving power of only 8.0 dBm, the linewidth increases from its intrinsic value of 0.62 kHz to 2.12 kHz, corresponding to a cooperativity $C = 2.4$. As a comparison, a driving power of 34 dBm is used to achieve the same cooperativity when the drive is applied off-resonance, indicating the drastic enhancement of the magnomechanical interaction induced by the triple-resonance condition. The reflection signal for the blue detuning situation is plotted in Fig. 4B at various driving powers. As the driving power increases, the center frequency of the small phonon–induced resonance inside the hybrid mode is blue-shifted, and its linewidth linearly decreases (Fig. 4C, blue circles).

A direct comparison of panels (A) and (B) in Fig. 4 reveals distinctly different spectral line shapes of the phonon-induced resonances. Same as with the case of the off-resonance drive, we observed MMIT for the red-detuned drive in the triple-resonant system, with the peak height and linewidth of the transparency window increasing with the driving power. For the blue-detuned drive, we observed the transition from MMIA to MMIT and then to MMPA, and eventually to self-sustained oscillation as we increased the driving power. These observations lead to a unified explanation about the modified spectral line shape (which is not limited to the triple-resonance situation): the coupling with phonon introduces additional dissipation and phase shift to the hybridized modes and therefore changes their line shapes. When the parametric drive is applied, the effective dissipation rate of the hybrid mode is modified from $\kappa$ to $\kappa(1\pm C)$, which increases for the



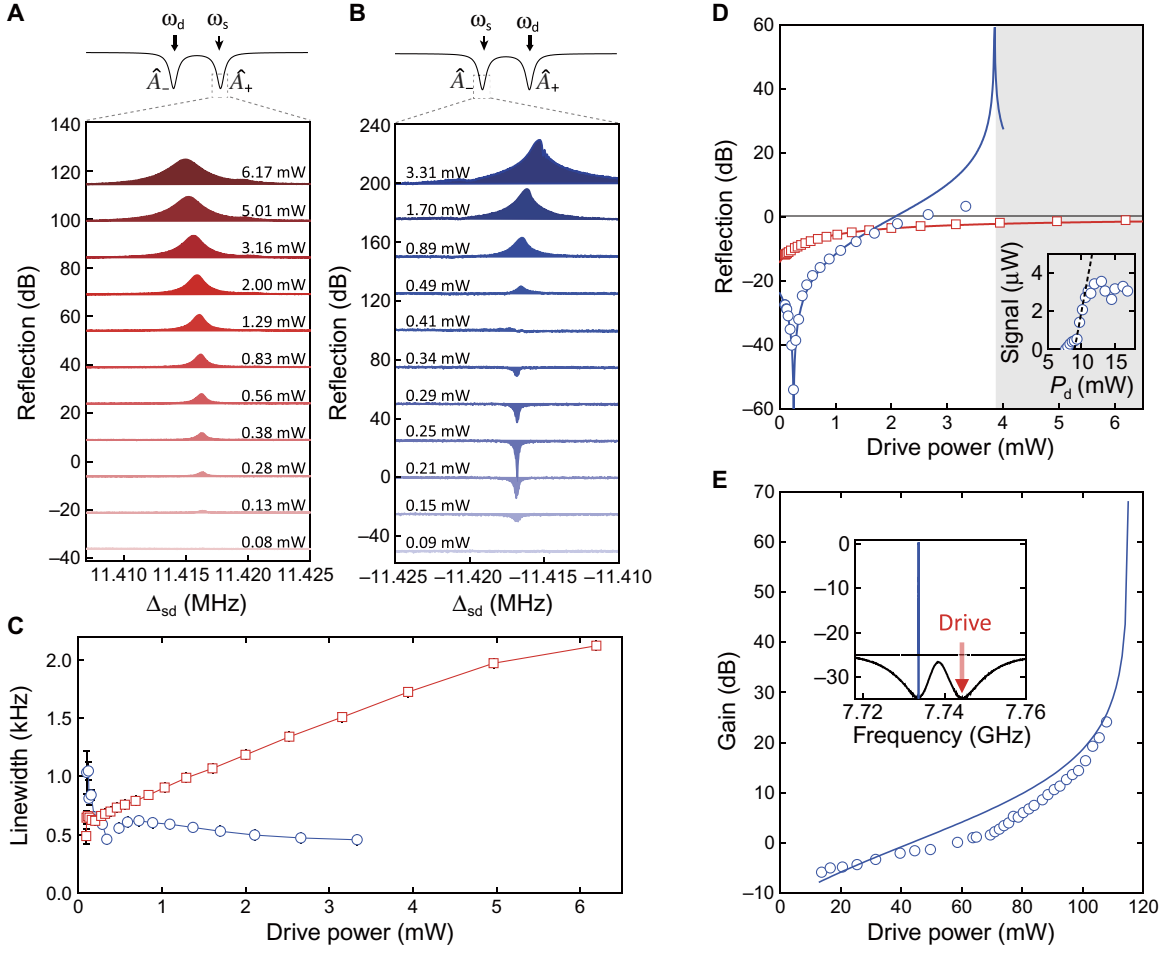


**Fig. 4. Enhanced magnomechanical coupling in the triple-resonant system.** (**A**) MMIT signal for a red-detuned drive at various driving powers. (**B**) MMIA and MMPA signal for a blue-detuned drive at various driving powers. (**C**) The linewidth of the magnomechanically induced resonance as a function of the drive power. (**D**) Magnomechanical interaction–modified on-resonance reflectivity of the hybrid mode as a function of the drive power. Shaded area indicates the instable regime. Inset: Measured power of the Stokes sideband of the driving signal. The threshold behavior indicates the onset of phonon lasing. (**E**) Magnomechanical parametric gain as a function of the drive power in an overcoupled hybrid system. Inset: Measured reflection spectrum that shows a 25-dB gain. In the main panels of (C) to (E), blue circles (red squares) are for the blue (red) detuning and solid lines are theoretical calculations.

red-detuned drive and decreases for the blue-detuned drive. Given a fixed external coupling rate $\kappa_e$, the on-resonance reflectivity of the cavity is

$$r = \frac{1 \pm C - 2\frac{\kappa_e}{\kappa}}{1 \pm C} \quad (3)$$

Therefore, depending on the external coupling condition and the driving power, the reflection spectra line shape varies among MMIT, MMIA, or MMPA (see the Supplementary Materials for more details).

The measured on-resonance reflectivity for an undercoupled hybrid mode agrees well with our theoretical model (Fig. 4D). For the red-detuned drive, the increasing linewidth with elevated driving power causes the mode to be further undercoupled, and therefore, the on-resonance reflectivity increases. On the contrary, for the blue-detuned situation, the decreasing linewidth first leads to critical coupling and then over-coupling condition, yielding a dip in the reflectivity followed by a rapid increase, which diverges as $C \approx 1$ at a driving power of 6.2 dBm. The deviation of the measured reflectivity from the theoretical prediction can be attributed to thermal instability or gain-bandwidth product limitation, which also limits the highest measurable parametric gain to 3 dB. When the hybrid mode is tuned to overcoupled, the increase of the parametric gain with the driving power is more gradual, and therefore, a much higher parametric gain up to 25 dB is achieved before reaching instability (Fig. 4E). The observed MMPA is similar to the electromechanical parametric amplifiers (*39*) but with unprecedented tunability. Further increasing the driving power leads the system into the instable regime where the phonon mode experiences self-sustained oscillation. The threshold behavior of the measured emission power from the Stokes sideband, as shown in the inset of Fig. 4D, indicates the onset of the phonon lasing (*23*).

## DISCUSSION

The demonstration of the coherent magnon-phonon interaction, including the MMIT (MMIA) and MMPA, provides a versatile platform for coherent information processing. Besides, because YIG also has great optical properties such as low optical loss and optomagnetic nonreciprocity, our study shows the potential for integrating different systems, including microwave, optical, mechanical, and magnonic systems, in a single device, and realizing information interconversion among these different information carriers. Distinguished from opto- or electromechanical systems, our cavity magnomechanical system shows a high level of tunability that allows the resonance to be externally controlled in a wide frequency range. Moreover, such a complex system is compatible with superconducting quantum circuits (*40*). All of these not only are crucial for realizing long-desired functions such as microwave-to-optical conversion (*15*–*17*, *41*, *42*) but also provide a flexible platform that intrigues the fundamental study of exotic magnetic excitations.

## MATERIALS AND METHODS

### Device description

The device used in our experiments consists of a three-dimensional microwave cavity and a YIG sphere (Fig. 1, A and B). The microwave cavity is machined from high-conductivity copper. With its inner dimension designed as $43 \times 21 \times 7.2$ mm$^3$, the copper cavity supports a $TE_{011}$ mode resonating at 7.8 GHz with a loaded $Q$ factor of about 2000. A 250-μm-diameter YIG sphere, serving as both the magnon and the phonon resonator, is glued at the end of 125-μm-diameter silica fiber for mechanical support. The YIG sphere is highly polished from pure single-crystal YIG to guarantee excellent microwave, magnonic, and mechanical performances. The sphere is mounted inside the copper cavity at the position where the microwave magnetic field of the $TE_{011}$ mode is strongest to ensure the strong coupling between magnon and microwave photon. A coaxial probe is used to access the cavity microwave photon for both the input and output.

### Measurement setup

Our measurement was carried out in air at room temperature. The measurement scheme is shown in Fig. 1E. The device is mounted between the two poles of a water-cooled electromagnet. The bias magnetic field is tuned by the electric current, and a Gaussmeter is used to monitor the applied magnetic field via a Hall probe. In our experiments, the bias field of the YIG sphere is above its saturation magnetization (1750 Oe), which guarantees the relatively low magnon dissipation rate and also helps to reduce the phonon damping. The frequency of the uniform magnon mode, which is linearly proportional to the bias magnetic field, can therefore be conveniently swept or precisely controlled. The probe signal, at a very low power level (−10 dBm), comes from a VNA. The driving signal is provided by a separate microwave source, which is first amplified and then combined with the probe signal using a directional coupler after going through a bandpass filter to eliminate any spurs or harmonics. A microwave power meter is used to record the drive power that is sent to the device. The insertion losses from all components (cable, device, directional coupler, etc.) are taken into account to calibrate the drive power in the device. The reflection output from the device is separated from the input signal using a circulator to avoid possible interferences and then sent back to the VNA to measure the amplitude and phase response of the device. A notch filter is used in front of the receiving port of the VNA to filter out the strong drive to avoid any undesired interference or receiver saturation. By applying the drive signal detuned from the hybrid mode by a frequency equal to the phonon frequency and by sweeping the probe frequency near the hybrid resonance, we could observe the coherent magnomechanical interaction.

## SUPPLEMENTARY MATERIALS

Supplementary material for this article is available at http://advances.sciencemag.org/cgi/content/full/2/3/e1501286/DC1

Magnomechanical interaction through magnetostrictive forces

Magnon modes of the YIG sphere

Coherent cavity magnomechanical coupling

Thermal instability

Table S1. Definitions and meanings of symbols.

Fig. S1. Magnetically induced transparency/absorption at various drive frequencies.

Fig. S2. Magnomechanical resonance line shape and parameter space diagram.

Fig. S3. Cascade transparency/absorption.

References (*43*–*52*)

## REFERENCES AND NOTES

1. M. Aspelmeyer, T. J. Kippenberg, F. Marquardt, Cavity optomechanics. *Rev. Mod. Phys.* **86**, 1391–1452 (2014).
2. T. J. Kippenberg, K. J. Vahala, Cavity opto-mechanics. *Opt. Express* **15**, 17172–17205 (2007).
3. M. Li, W. H. P. Pernice, C. Xiong, T. Baehr-Jones, M. Hochberg, H. X. Tang, Harnessing optical forces in integrated photonic circuits. *Nature* **456**, 480–484 (2008).

4. Y.-S. Park, H. Wang, Resolved-sideband and cryogenic cooling of an optomechanical resonator. *Nat. Phys.* **5**, 489–493 (2009).
5. S. Weis, R. Rivière, S. Deléglise, E. Gavartin, O. Arcizet, A. Schliesser, T. J. Kippenberg, Optomechanically induced transparency. *Science* **330**, 1520–1523 (2010).
6. A. H. Safavi-Naeini, T. P. Mayer Alegre, J. Chan, M. Eichenfield, M. Winger, Q. Lin, J. T. Hill, D. E. Chang, O. Painter, Electromagnetically induced transparency and slow light with optomechanics. *Nature* **472**, 69–73 (2011).
7. J. T. Hill, A. H. Safavi-Naeini, J. Chan, O. Painter, Coherent optical wavelength conversion via cavity optomechanics. *Nat. Commun.* **3**, 1196 (2012).
8. T. Carmon, H. Rokhsari, L. Yang, T. J. Kippenberg, K. J. Vahala, Temporal behavior of radiation-pressure-induced vibrations of an optical microcavity phonon mode. *Phys. Rev. Lett.* **94**, 223902 (2005).
9. T. J. Kippenberg, H. Rokhsari, T. Carmon, A. Scherer, K. J. Vahala, Analysis of radiation-pressure induced mechanical oscillation of an optical microcavity. *Phys. Rev. Lett.* **95**, 033901 (2005).
10. H. Rokhsari, T. J. Kippenberg, T. Carmon, K. J. Vahala, Radiation-pressure-driven micromechanical oscillator. *Opt. Express* **13**, 5293–5301 (2005).
11. O. Arcizet, P.-F. Cohadon, T. Briant, M. Pinard, A. Heidmann, Radiation-pressure cooling and optomechanical instability of a micromirror. *Nature* **444**, 71–74 (2006).
12. S. Gigan, H. R. Böhm, M. Paternostro, F. Blaser, G. Langer, J. B. Hertzberg, K. C. Schwab, D. Bäuerle, M. Aspelmeyer, A. Zeilinger, Self-cooling of a micromirror by radiation pressure. *Nature* **444**, 67–70 (2006).
13. A. Schliesser, P. DelHaye, N. Nooshi, K. J. Vahala, T. J. Kippenberg, Radiation pressure cooling of a micromechanical oscillator using dynamical backaction. *Phys. Rev. Lett.* **97**, 243905 (2006).
14. J. D. Teufel, D. Li, M. S. Allman, K. Cicak, A. J. Sirois, J. D. Whittaker, R. W. Simmonds, Circuit cavity electromechanics in the strong-coupling regime. *Nature* **471**, 204–208 (2011).
15. R. W. Andrews, R. W. Peterson, T. P. Purdy, K. Cicak, R. W. Simmonds, C. A. Regal, K. W. Lehnert, Bidirectional and efficient conversion between microwave and optical light. *Nat. Phys.* **10**, 321–326 (2014).
16. T. Bagci, A. Simonsen, S. Schmid, L. G. Villanueva, E. Zeuthen, J. Appel, J. M. Taylor, A. Sørensen, K. Usami, A. Schliesser, E. S. Polzik, Optical detection of radio waves through a nanomechanical transducer. *Nature* **507**, 81–85 (2014).
17. J. Bochmann, A. Vainsencher, D. D. Awschalom, A. N. Cleland, Nanomechanical coupling between microwave and optical photons. *Nat. Phys.* **9**, 712–716 (2013).
18. L. Fan, K. Y. Fong, M. Poot, H. X. Tang, Cascaded optical transparency in multimode-cavity optomechanical systems. *Nat. Commun.* **6**, 5850 (2015).
19. M. Zahn, *Derivation of the Korteweg-Helmholtz electric and magnetic force densities including electrostriction and magnetostriction from the quasistatic Poynting's theorems*, 2006 IEEE Conference on Electrical Insulation Dielectric Phenomena, Kansas City, MO, 15 to 18 October 2006.
20. A. A. Serga, A. V. Chumak, B. Hillebrands, YIG magnonics. *J. Phys. D Appl. Phys.* **43**, 264002 (2010).
21. B. Lenk, H. Ulrichs, F. Garbs, M. Münzenberg, The building blocks of magnonics. *Phys. Rep.* **507**, 107–136 (2011).
22. A. V. Chumak, V. I. Vasyuchka, A. A. Serga, B. Hillebrands, Magnon spintronics. *Nat. Phys.* **11**, 453–461 (2015).
23. E. G. Spencer, R. C. LeCraw, Magnetoacoustic resonance in yttrium iron garnet. *Phys. Rev. Lett.* **1**, 241–243 (1958).
24. S. Wang, T.-I. Hsu, Spin-wave experiments: Parametric excitation of acoustic waves and mode-locking of spin waves. *Appl. Phys. Lett.* **16**, 111–113 (1970).
25. A. V. Scherbakov, A. S. Salasyuk, A. V. Akimov, X. Liu, M. Bombeck, C. Brüggemann, D. R. Yakovlev, V. F. Sapega, J. K. Furdyna, M. Bayer, Coherent magnetization precession in ferromagnetic (Ga,Mn)As induced by picosecond acoustic pulses. *Phys. Rev. Lett.* **105**, 117204 (2010).
26. J.-W. Kim, M. Vomir, J.-Y. Bigot, Ultrafast magnetoacoustics in nickel films. *Phys. Rev. Lett.* **109**, 166601 (2012).
27. O. Kovalenko, T. Pezeril, V. V. Temnov, New concept for magnetization switching by ultrafast acoustic pulses. *Phys. Rev. Lett.* **110**, 266602 (2013).
28. V. V. Temnov, Ultrafast acousto-magneto-plasmonics. *Nat. Photonics* **6**, 728–736 (2012).
29. J. Janušonis, C. L. Chang, P. H. M. van Loosdrecht, R. I. Tobey, Frequency tunable surface magneto elastic waves. *Appl. Phys. Lett.* **106**, 181601 (2015).
30. F. Hocke, X. Zhou, A. Schliesser, T. J. Kippenberg, H. Huebl, R. Gross, Electromechanically induced absorption in a circuit nano-electromechanical system. *New J. Phys.* **14**, 123037 (2012).
31. Y. Tabuchi, S. Ishino, T. Ishikawa, R. Yamazaki, K. Usami, Y. Nakamura, Hybridizing ferromagnetic magnons and microwave photons in the quantum limit. *Phys. Rev. Lett.* **113**, 083603 (2014).
32. X. Zhang, C.-L. Zou, L. Jiang, H. X. Tang, Strongly coupled magnons and cavity microwave photons. *Phys. Rev. Lett.* **113**, 156401 (2014).
33. M. Goryachev, W. G. Farr, D. L. Creedon, Y. Fan, M. Kostylev, M. E. Tobar, High-cooperativity cavity QED with magnons at microwave frequencies. *Phys. Rev. Appl.* **2**, 054002 (2014).
34. L. Bai, M. Harder, Y. P. Chen, X. Fan, J. Q. Xiao, C.-M. Hu, Spin pumping in electrodynamically coupled magnon-photon systems. *Phys. Rev. Lett.* **114**, 227201 (2015).
35. G. Kurizki, P. Bertet, Y. Kubo, K. Mølmer, D. Petrosyan, P. Rabl, J. Schmiedmayer, Quantum technologies with hybrid systems. *Proc. Natl. Acad. Sci. U.S.A.* **112**, 3866–3873 (2015).
36. N. Bergeal, F. Schackert, M. Metcalfe, R. Vijay, V. E. Manucharyan, L. Frunzio, D. E. Prober, R. J. Schoelkopf, S. M. Girvin, M. H. Devoret, Phase-preserving amplification near the quantum limit with a Josephson ring modulator. *Nature* **465**, 64–68 (2010).
37. V. Fiore, Y. Yang, M. C. Kuzyk, R. Barbour, L. Tian, H. Wang, Storing optical information as a mechanical excitation in a silica optomechanical resonator. *Phys. Rev. Lett.* **107**, 133601 (2011).
38. R. C. LeCraw, E. G. Spencer, E. I. Gordon, Extremely low loss acoustic resonance in single-crystal garnet spheres. *Phys. Rev. Lett.* **6**, 620–622 (1961).
39. F. Massel, T. T. Heikkilä, J.-M. Pirkkalainen, S. U. Cho, H. Saloniemi, P. J. Hakonen, M. A. Sillanpää, Microwave amplification with nanomechanical resonators. *Nature* **480**, 351–354 (2011).
40. Y. Tabuchi, S. Ishino, A. Noguchi, T. Ishikawa, R. Yamazaki, K. Usami, Y. Nakamura, Coherent coupling between a ferromagnetic magnon and a superconducting qubit. *Science* **349**, 405–408 (2015).
41. S. Barzanjeh, M. Abdi, G. J. Milburn, P. Tombesi, D. Vitali, Reversible optical-to-microwave quantum interface. *Phys. Rev. Lett.* **109**, 130503 (2012).
42. Y.-D. Wang, A. A. Clerk, Using interference for high fidelity quantum state transfer in optomechanics. *Phys. Rev. Lett.* **108**, 153603 (2012).
43. J. P. Joule, On a new class of magnetic forces. *Ann. Electr. Magn. Chem.* **8**, 219–224 (1842).
44. A. G. Gurevich, G. A. Melkov, *Magnetization oscillations and waves* (CRC Press, Boca Raton, FL, 1996).
45. H. Keshtgar, M. Zareyan, G. E. W. Bauer, Acoustic parametric pumping of spin waves. *Solid State Commun.* **198**, 30–34 (2014).
46. A. N. Cleland, *The Foundations of Nanomechanics: From Solid-State Theory to Device Applications* (Springer-Verlag, New York, 2003).
47. N. Nishiguchi, T. Sakuma, Vibrational spectrum and specific heat of fine particles. *Solid State Commun.* **38**, 1073–1077 (1981).
48. D. F. Gibbons, V. G. Chirba, Acoustical loss and Young's modulus of yttrium iron garnet. *Phys. Rev.* **110**, 770–771 (1958).
49. A. E. Clark, R. E. Strakna, Elastic constants of single-crystal YIG. *J. Appl. Phys.* **32**, 1172–1173 (1961).
50. E. H. Turner, Interaction of phonons and spin waves in yttrium iron garnet. *Phys. Rev. Lett.* **5**, 100–101 (1960).
51. R. E. Tokheim, G. Johnson, Optimum thermal compensation axes in YIG and GaYIG ferrimagnetic spheres. *IEEE Trans. Magn.* **7**, 267–276 (1971).
52. Y. A. Burenkov, S. P. Nikanorov, Temperature effect on the elastic properties of yttrium garnet ferrite $Y_3Fe_5O_{12}$. *Phys. Solid State* **44**, 318–323 (2002).


**Acknowledgments:** We thank N. Zhu for gluing the YIG sphere to the silica fiber. **Funding:** This work was supported by the Defense Advanced Research Projects Agency (DARPA) Microsystems Technology Office/Mesodynamic Architectures program (N66001-11-1-4114). C.-L.Z., L.J., and H.X.T. acknowledge support from Laboratory Physical Sciences (LPS) through an Army Research Office (ARO) grant (W911NF-14-1-0563), from an Air Force Office of Scientific Research (AFOSR) Multidisciplinary University Research Initiative grant (FA9550-15-1-0029), and from Packard Foundation. L.J. also acknowledges support from the Alfred P. Sloan Foundation. **Author contributions:** X.Z. prepared the sample and performed the measurement and data analysis. C.-L.Z and L.J. provided theoretical analysis. H.X.T. supervised the project. All authors contributed to the writing of the manuscript. **Competing interests:** The authors declare that they have no competing interests. **Data and materials availability:** All data needed to evaluate the conclusions in the paper are present in the paper and/or the Supplementary Materials. Additional data related to this paper may be requested from the authors.

Submitted 16 September 2015
Accepted 13 January 2016
Published 18 March 2016
10.1126/sciadv.1501286

**Citation:** X. Zhang, C.-L. Zou, L. Jiang, H. X. Tang, Cavity magnomechanics. *Sci. Adv.* **2**, e1501286 (2016).

ScienceAdvances

# Cavity magnomechanics

Xufeng Zhang, Chang-Ling Zou, Liang Jiang, and Hong X. Tang

*Sci. Adv.* **2** (3), e1501286. DOI: 10.1126/sciadv.1501286







*Science Advances* (ISSN 2375-2548) is published by the American Association for the Advancement of Science. 1200 New York Avenue NW, Washington, DC 20005. The title *Science Advances* is a registered trademark of AAAS.